P.R. van der Wilt

Euler-Lagrange Simulation of Glycolytic Oscillations using the Lattice Boltzmann Method

TU Delft

Euler-Lagrange Simulation of Glycolytic Oscillations using the Lattice Boltzmann Method

By

P.R. van der Wilt

in partial fulfilment of the requirements for the degree of

Bachelor of Science
in Life Sciences and Technology

at the Delft University of Technology,
to be defended publicly on Monday November 21, 2022, at 1:00 PM.

Supervisor: Dr. ir. C. Haringa
Thesis committee: Dr. ir. M.E. Klijn, TU Delft

TU Delft

Preface

I would like to thank dr. ir. Cees Haringa for taking the time to provide supervision, feedback, and guidance during my Bachelor End Project despite his busy schedule. Without his suggestions and expertise, this project would not have reached completion. I would also like to thank dr. ir. Marieke Klijn for being my second corrector and for teaching Transport Phenomena which is what lead to me doing my BEP at the BPE section. Finally, I would like to thank the BPE section for providing suggestions, support, and the occasional cake during my time as BEP student. I thoroughly enjoyed my time at the BPE section and hope to learn more about the field during my upcoming LST master's program.

Pieter van der Wilt
Delft, November 2022

Abstract

The traditional Eulerian view of biomass in bioprocess modelling results in issues when modelling large-scale bioreactors in which heterogeneous conditions are common. As the field increasingly moves from "scale-up" to "scale-down" philosophy, in which such heterogeneities are included from the start of process design, accurate modelling of the biomass response to these varying conditions is essential. Euler-Lagrange (*EL*) simulations provide a means of modelling the microbial lifelines of cells traversing heterogenous conditions of a bioreactor.

Lapin et al. were the pioneers of *EL* simulation in their 2004 paper where a metabolic model of glycolysis is coupled to a Lagrangian biomass phase. This BSc thesis focusses on reproducing their model using modern computational fluid dynamics (*CFD*) techniques. Specifically, by using a dynamic Lattice Boltzmann Method using Large Eddy Simulation model for *CFD* as opposed to a frozen-flow Finite Volume Reynolds Averaged Navier-Stokes model. The resulting differences in the overall behaviour of the cell metabolism through the lens of glycolytic oscillations are discussed. In addition, possible pitfalls in model validity such as grid dependence, the effects of heterogeneous particle distributions and the effects of particle numbers were explored. The synchronisation and desynchronisation of glycolytic oscillations as observed in Lapin et al. 2004 were able to be reproduced.

Abbreviations: **CFD**, Computational Fluid Dynamics; **DRW**, Discrete Random Walk; **EL**, Euler-Lagrange; **FV**, Finite Volume method; **PRNG**, Pseudorandom Number Generator; **RANS**, Reynolds Averaged Navier Stokes; **LBM**, Lattice Boltzmann Method; **LES**, Large Eddy Simulation

Table of Contents

Introduction

As the design philosophy behind industrial fermenters has increasingly shifted from a "scale-up" to a "scale-down" approach over the last 25 years, the usage of computational fluid mechanics (*CFD)* for modelling large-scale reactor conditions has gained increasing attention. The seminal papers by Lapin et al. (2004, 2006) introduced an essential tool in these kind of large-scale bioprocess simulations by successfully implementing Euler-Lagrange (*EL*) methods for modelling the heterogeneous conditions experienced by micro-organisms and the resulting metabolic effects. Since the introduction of *EL* simulations, many optimisations for exploring the lifelines of cells through different metabolic regimes have been explored, such as arc-time and Fourier analysis (Haringa et al., 2016). However, a notable absence is literature concerns models like Lapin's model, implementing metabolic network modelling and two-way coupling between a metabolic network and scalar concentrations in the Eulerian phase. Most models in literature rely on an implementation where the metabolic rates are purely dependent on the instantaneous scalar concentration using Monod kinetics, instead of the state of metabolic network as a result of the cell's history (Haringa, Mudde, et al., 2018), (Monod, 1949).

The Finite Volume method using Reynolds Averaged Navier Stokes (*FV RANS*) are most often used to model the static flow fields for *EL* simulations. The advantage of using these steady state, frozen fluid models is the ability to keep computation times low. However, this comes at the cost of the absence of relevant dynamic phenomena such as macro-instability vortices which are relevant for computing accurate mixing times (Haringa, Vandewijer, et al., 2018a), (Haringa, Vandewijer, et al., 2018b). Dynamic *FV RANS* simulations which do include these phenomena are extremely computationally demanding with computation times on the order of weeks.

An alternative to *FV RANS* is the Lattice Boltzmann Method (*LBM*). *LBM* can produce dynamic flow fields Large Eddy Simulations (*LES*) at similar computation times as static *FV RANS* simulations due to developments in parallel computing on Graphical Processing Units. Combined with the recent releases of both commercial and open-source software for *LBM* simulations, this has improved the ease of application in research significantly. Thus far, most research using *LBM* has focused on the study of transport phenomena due to the superior performance in modelling relevant dynamic phenomena in mixing and mass transfer. Studies applying 2-way coupled kinetic models in an *LBM* simulation have yet to emerge.

This bachelor thesis seeks to reproduce the results of Lapin et al. 2004 using *LBM* simulation and to show that two-way coupled *EL* simulations with metabolic network simulation are feasible using this method. Lapin's model explored reactor heterogeneity via glycolytic oscillations in yeast, which we shall attempt to replicate. We will compare the differences between the original model and *LBM* model in terms of both setup and results. We will also explore the pitfalls in model validity influencing the results, such as grid dependence, the effects of heterogeneous particle distributions and the effects of particle numbers.

Nomenclature

Latin

a	PRNG multiplication parameter
arg	Argument of complex number
c	Concentration, M
C_s	Smagorinsky coefficient
d	Diameter, m
D	Diffusion coefficient, $m^2\ s^{-1}$
D_t	Eddy diffusivity, $m^2\ s^{-1}$
e	Euler's number
f	Particle distribution function
$\vec{F}$	External forces on fluid, N
H	Hilbert transform
i	Imaginary unit number
m	PRNG modulus parameter
M	Chemical amount, mol
N_p	Total number of particles
N_{imp}	Impeller revolutions, RPM
N_s	No sampled particles
P	Impeller power, W
PDF	Probabilty density function
Po	Power number
r	Distance between particles
$\bar{r}$	Mean Nearest Neighbour distance
R	Kuramoto order parameter
Re_{imp}	Impeller Reynolds number
$\bar{S}$	Filtered rate of strain
Sc_t	Turbulent Schmidt number
Stk	Stokes number
t	Time, s
$\vec{v}$	Phase space velocity
V	Volume, m^3
$\vec{u}_{tip}$	Impeller tip velocity, $m\ s^{-1}$
x	NADH signal, M
$\tilde{x}$	Hilbert transform of signal
x_a	Analytical signal
X_n	Pseudorandom number
X_s	PRNG seed

Greek

δ	Dirac delta function
Δ_x	Spatial resolution, m
Δ_t	Temporal resolution, s
ν_t	Eddy viscosity, $m^2\ s^{-1}$
ρ	Density, $kg\ m^{-3}$
φ	Phase
Ω	Collision operator
ω_{imp}	Angular velocity impeller, s^{-1}

Other

∇	Gradient
$\nabla\cdot$	Divergence
$\frac{d}{dt}$	Derivative in time
$\frac{\partial}{\partial t}$	Partial derivative in time

Subscripts

ex	Extracellular
f	Fluid
imp	Impeller
m	Intracellular
p	Particle
t	Turbulent
x	Spatial
ϵ	Energy dissipation

Literature & Methods

Glycolytic oscillations

The Embden–Meyerhof–Parnas glycolytic pathway is responsible for the conversion of glucose into pyruvate in many organisms. Glycolysis is common among many different species, having been conserved from bacteria all the way to humans. Certain conditions can induce oscillations in the glycolytic metabolic pathways (Bier et al., 2000). One particularly useful feature of these oscillations is that under certain conditions, groups of cells will synchronise their oscillations. This has been observed in everything from bacteria to the human pancreas (Schaefer et al., 1999), (Bertram et al., 2010). Glycolytic synchronisation is thought to be mediated via by-products of glycolysis such as acetaldehyde and pyruvate (Madsen et al., 2005). Yeast cells will tend to synchronise at high volume fractions with adequate mixing. Conversely, heterogeneity in the acetaldehyde / pyruvate concentration due to poor mixing and low volume fractions can lead to the desynchronisation of cell populations (Weber et al., 2012). Therefore, the glycolytic oscillations of yeast provide a good model for exploring reactor heterogenicity and therefore used as such in Lapin's 2004 paper on the implementation of *EL* simulation.

Lapin 2004 model

The Lapin 2004 model uses a *FV RANS* model with a modified Chen-Kim k-ε turbulence model in the commercial *CFD* software PHOENICS to model the frozen flow field. The convective movement of the particles of the Lagrangian phase is modelled assuming that they are fully flow-following. On top of the convective movement in accordance with the frozen flow field, a discrete random walk (*DRW*) model is implemented to model effect of turbulent dispersion on the Lagrangian phase. It should be noted that the *DRW* model tends to produce unrealistically long residence times at the model boundaries. This resulted in a heterogeneous particle distribution of the Lagrangian phase as noted by Lapin et al. in a later paper (Lapin et al., 2006).

In terms of scalar transport, the Reynolds assumption is used, meaning the turbulent Schmidt number Sc_t is assumed to be at unity (equation 1). The Reynolds assumption tends to be an overestimation of Schmidt number which is generally between 0.1 and 1 in water-based systems (Gualtieri et al., 2017). Subsequently, the eddy diffusivity D_t is underestimated resulting in slower turbulent diffusion.

(1) $$Sc_t = \frac{\nu_t}{D_t} = 1$$

Lapin does not use a quantitative method to describe the degree of synchronisation, instead graphing the NADH concentrations over time and determining the degree of synchronisation and desynchronisation qualitatively. The desynchronised oscillations are not uniformly distributed judging by the NADH graph in figure 1. This indicates that only partial desynchronisation occurs in Lapin's model.

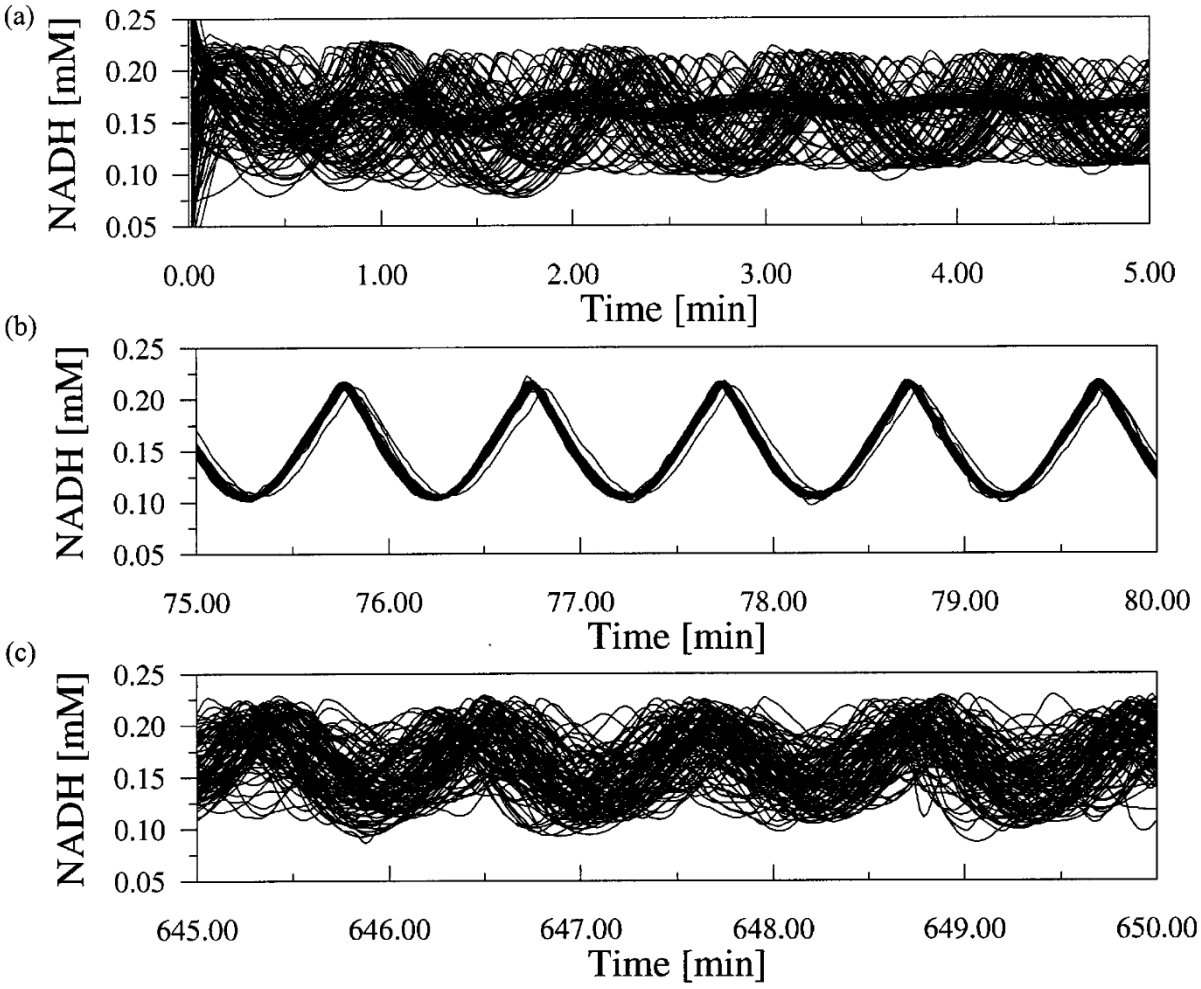

Figure 1. Synchronisation of the glycolytic oscillations with nonideal mixing. The intracellular NADH concentration is shown for 100 of the 10^5 simulated cells. (a) Disorganised oscillations 5 minutes after the start of the simulation with a desynchronised population at a stirring speed of N_{imp} = 165 RPM. (b) Synchronised oscillations after 70 min for the same settings. (c) Same simulation as in b, but after switching to a stirring speed of N_{imp} = 55 RPM at t = 80 min; a partial desynchronisation of oscillations is observed after 600 minutes. [Reprinted with permission from Lapin et al. Ind. Eng. Chem. Res. 2004, 43, 16, 4647–4656, Copyright © 2004 American Chemical Society.]

Current Model Implementation

All simulations were performed in M-Star CFD version 3.7.64 (M-Star Simulations LLC) on a XEON-W2265 windows desktop using a NVIDIA RTX3090 24GB GPU and a TOSHIBA DT01ACA200 2TB HDD for storage.

The baffled tank / stirrer geometry and fluid parameters (table 1) are based on Lapin et al. 2004 paper which are in turn based on experimental papers by Costes and Couderc (1982, pp. 25–34), (1988). A Rushton impeller was used to stir the tank. The fluid used is waterlike, thus the density and viscosity are set close to those of water and a Newtonian viscosity model was used. The initial fluid pressure is set to standard atmospheric pressure.

Table 1. Tank geometry and fluid parameters used in simulations. The tank geometry was given by Costes and Couderc (1988).

Parameter	Value	Parameter	Value
Tank height	0.44 m	4 x baffles width	0.044 m
Tank diameter	0.44 m	Fluid density	1000 kg m^3
Height of impeller above tank floor	0.22 m	Fluid kinematic viscosity	10^{-6} m^2 s^{-1}
Impeller diameter	0.147 m	Initial fluid pressure	101325 Pa

Lattice Boltzmann Method & Large Eddy Simulation

The basis of the *LBM* is the Boltzmann transport equation. This equation ties a molecular probability density function f of the fluid to the phase space velocity $\vec{v}$, external forces $\vec{F}$ and the collision parameter Ω according to equation 2. This statistical fluid description contrasts with the traditional Navier-Stokes equations describing fluid motion.

$$\frac{\partial f}{\partial t} + \vec{v}\nabla_x f + \vec{F}\nabla_{\vec{v}} f = \Omega(f, f) \quad (2)$$

Discretising the control volume into a discrete phase space lattice and finding a suitable collision operator (D3Q19 discretisation and BGK operator in this case) allows the formula to be solved numerically. For further details regarding the *LBM*, refer to M-Star's documentation (M-Star Simulations LLC, 2022) or Krüger et al.'s book on the subject (2006).

The local fluid density is calculated from the molecular PDF f. Inadequate simulation settings can result in non-physical fluctuations in local fluid density, whereas a constant density is expected due to the incompressible nature of water-like fluids. To restrict local density fluctuation to a maximum of 1% a Courant number (equation 3) of 0.05 is chosen (Thomas et al., 2021), (Haringa, 2022).

(3) $$Co = \vec{u}_{tip}\frac{\Delta_t}{\Delta_x} = 0.05$$

A Large Eddy Simulation (*LES*) turbulence model is applied to the simulation according to equation 4 with a Smagorinsky coefficient C_s of 0.1 (Gillissen & Van den Akker, 2012). *LES* adds the unresolved turbulence effects through modelling the sub-grid local eddy viscosity ν_t as a function of the filtered rate of strain $\bar{S}$.

(4) $$\nu_t = (C_s\Delta_x)^2\bar{S}$$

The sub-grid local eddy viscosity is added to the molecular viscosity to account for the effects of unresolved eddies with length scales smaller than the simulation resolution on the flow dynamics (Pope, 2000). Though these unresolved eddies also affect mass transfer via a sub-grid local turbulent diffusion coefficient D_t, this effect is not modelled in M-Star's implementation of *LES* according to communications with M-Star Simulations LLC.

M-Star CFD configuration

The *LBM* uses a Cartesian grid; thus, any curved geometries lead to stair-stepping. This can lead to artificial flows near the geometry. Boundary interpolation schemes improve model accuracy especially at lower resolutions by mitigating the stair stepping of the lattice grid (Osaki et al., 2021). Therefore, the baffled tank geometry employs M-Star's interpolation scheme as opposed to being aligned to the Cartesian lattice.

The vessel walls are no-slip surfaces except the top surface which is a free-slip surface. The top being a free-surface simulates the negligible friction of the air-water interface. Not resolving the free surface reduces the computational costs, while having little effect on model accuracy (Nagaosa, 1999). Moving bodies are accounted for using the immersed boundary method with a no-slip boundary condition.

The biomass phase is modelled using a Lagrangian approach as is the basis of *EL* simulations. Therefore, the cells are modelled as virtual particles representing a collection of cells which are referred to as parcels. In this text, parcel and particle will be used interchangeably. The biomass phase was implemented using the Solids object in M-Star. A Tracer object is preferred; however, M-Star does not support on particle reactions on massless tracers at this time. To approach massless behaviour with the inertial particle approach, the particle density ρ_p was set at 1000 kg m^{-3}, equivalent to the surrounding fluid, and buoyancy / gravity forces were disabled.

The metabolic network is implemented with the OnParticleReaction object containing the metabolic equations which compute the metabolic rates, with each intracellular species being ReactionSpecies objects contain the concentrations. Since this study focuses on the synchronisation of metabolic oscillations, the parcel population must initialise in heterogeneous metabolic state. In accordance with Lapin 2004, the metabolic species concentrations of the parcels are set to a uniform distribution between zero and twice the mean concentration found on the oscillatory solution. The mean initial values are shown in table 2.

Table 2. Initial values for the intracellular reaction species for a point on the oscillatory solution corresponding to Table 3 as given by Lapin et al.

Variable	**Value**	**Variable**	**Value**
Glucose	1.023 mM	Acetaldehyde / Pyruvate	1.094×10^{-1} mM
G3P/DHP	6.696×10^{-1} mM	NADH	1.624×10^{-1} mM
1,3-BPG	7.194×10^{-2} mM	ATP	1.250 mM

However, since the ReactionSpecies are initialised at the same value for all parcels, a User Defined Function and *pseudorandom number generator* (*PRNG*) were required to set the random individual initial values. A *PRNG* is not a native feature in the M-Star User Defined Function API. The position of the particles at initialisation is random, therefore the position of the particle is used as a source of entropy for the *PRNG*.

First, the particle position in the x dimension is converted bitwise from a floating-point number to a 32-bit unsigned integer X_s. Subsequently, this integer is used as a seed for a cubic congruential generator (equation 5) which is normalised to produce a pseudorandom number $X_n \in [0, 1)$ (Eichenauer-Herrmann & Herrmann, 1997). This is repeated for the particle position in every dimension.

$$X_n = \frac{(aX_s)^3 \; mod \; m}{m} \tag{5}$$

$$a = 15{,}485{,}863;$$

$$m = 214{,}748{,}368$$

The modulus variable m was chosen for being close to $\frac{1}{20}$ of the maximum value of the 32-bit unsinged integer datatype and for being able to be stored in a single float. In hindsight, needing a modulus operator is unnecessary due to the overflow of the 32-bit unsigned integer having the same effect as a modulus operator. In fact, m needing to be close to an integer fraction of the maximum datatype value was a result of the modulus effects of overflow. Besides, due to limitations in float precision,

this approximate fraction leads to rounding errors as seen by increased probability densities around 0 and 1.

It should be noted that the cubic congruential generator was chosen for ease of implementation and low computational burden, not quality of randomness. However, poor quality randomness affecting the results is unlikely, owing to the chaotic movement of particles through the turbulent flow. The uniformity of the *PRNG* is depicted in figure 2. The distribution is statistically uniform as shown by a Kolmogorov-Smirnov test with 0.0505 as the p-value.

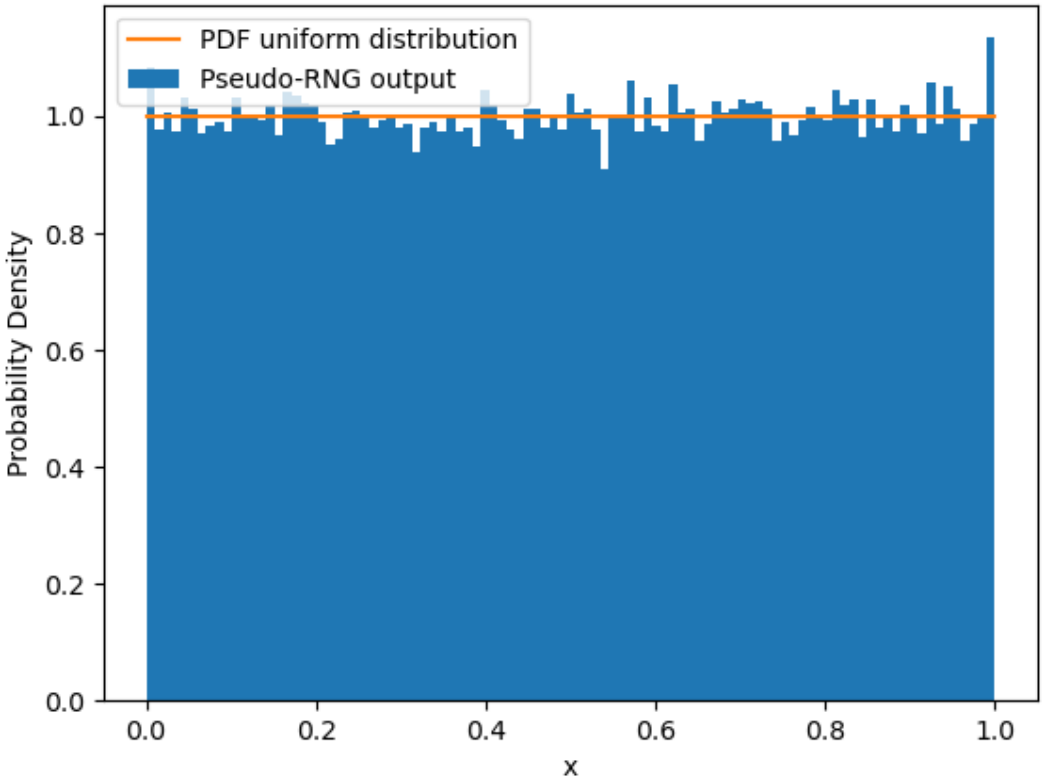

Figure 2. Output of the pseudo-random number generator compared to a uniform distribution. The Kolmogorov-Smirnov test results in a p-value of 0.0505.

The metabolic network is based on the Yeast-Cell-Ensemble model by Wolf and Heinrich (2000) and Henson et al. (2002). The model has a constant glucose flux J_0 into the cell and a variable acetaldehyde / pyruvate flux J_m based on concentrations either side of the cell membrane. The metabolic equations used in the model are labelled equations 6 and 7. The kinetic parameter values are shown in table 3. Notably, the model is based on a simplified glycolysis metabolic network. The kinetic parameters were chosen with the express purpose to produce glycolytic oscillation and are not based on experimental measurement of yeast glycolytic metabolism. The code of the metabolic network can be found in appendix 1. Due to the

non-linear nature of the metabolic equations, the RK4 integration method is used.

$$r_{1,m} = k_1 c_{Glu,m} c_{ATP,m} \left[1 + \left(\frac{c_{ATP,m}}{K_I}\right)^Q\right]^{-1} \quad (6.1)$$

$$r_{2,m} = k_2 c_{G3P,m}(c_{NADH,totm} - c_{NADH,m}) \quad (6.2)$$

$$r_{3,m} = k_3 c_{BPG,m}(c_{ATP,totm} - c_{ATP,m}) \quad (6.3)$$

$$r_{4,m} = k_4 c_{AP,m} c_{NADH,m} \quad (6.4)$$

$$r_{5,m} = k_5 c_{ATP,m} \quad (6.5)$$

$$r_{6,m} = k_6 c_{G3P,m} c_{NADH,m} \quad (6.6)$$

$$\frac{dc_{Glu,m}}{dt} = J_0 - r_{1,m} \quad (7.1)$$

$$\frac{dc_{G3P,m}}{dt} = 2r_{1,m} - r_{2,m} - r_{6,m} \quad (7.2)$$

$$\frac{dc_{BPG,m}}{dt} = r_{2,m} - r_{3,m} \quad (7.3)$$

$$\frac{dM_{AP,m}}{dt} = V_p \frac{dc_{AP}}{dt} = V_p(r_{3,m} - r_{4,m} - J_m) \quad (7.4)$$

$$\frac{dc_{NADH,m}}{dt} = r_{2,m} - r_{4,m} - r_{6,m} \quad (7.5)$$

$$\frac{dc_{ATP,m}}{dt} = -2r_{1,m} + 2r_{3,m} - r_{5,m} \quad (7.6)$$

Table 3. Kinetic parameter values as given by Lapin et al. after the Yeast-Cell-Ensemble model by Wolf and Heinrich and Henson et al. An error in the units of k_4 has been corrected.

Parameter	Value	Parameter	Value
J_0	2.30 mM min^{-1}	k	1.30 min^{-1}
k_1	100 mM^{-1} min^{-1}	κ	50.0 min^{-1}
k_2	6.00 mM^{-1} min^{-1}	Q	4.00
k_3	16.0 mM^{-1} min^{-1}	K_I	0.520 mM
k_4	100 mM^{-1} min^{-1}	$c_{NADH,mtot}$	1.00 mM
k_5	1.28 min^{-1}	$c_{ATP,mtot}$	4.00 mM
k_6	12.0 mM^{-1} min^{-1}		

The extracellular concentration of acetaldehyde and pyruvate $c_{AP,ex}$ is represented using a Scalar object and set at 8.419 × 10^{-2} mM. The molecular diffusion coefficient D is left at the default 10^{-9} m^2 s^{-1} as this is within the general order of magnitude for dilute solutes and the exact value is irrelevant under turbulent conditions. The degradation of

acetaldehyde / pyruvate is implemented using a Reaction object with the Euler integration method since this is adequate for the first-order reaction. The scalar transport through the cell membrane and the extracellular breakdown at any location in the control volume $\vec{x}$ occur according to equations 8 and 9. The transport of the scaler due to fluid motion is governed by the convection-diffusion equation (equation 10) with a Van Leer flux limiter to prevent numerical dispersion. The sink term S represents the reaction term at that location in the control volume.

(8) $$J_m = \kappa(c_{AP,m} - c_{AP,ex})$$

(9) $$\frac{dc_{AP,ex}}{dt} = -kc_{AP,ex} + \sum_m^{N_p} V_{p,m} J_m \delta(\vec{x} - \vec{x}_j) = S(\vec{x})$$

(10) $$\frac{\partial c}{\partial t} = \nabla \cdot (D \nabla c) - \nabla \cdot (\vec{v} c) + S$$

Kuramoto model

The Kuramoto model, first introduced by Shinomoto and Kuramoto, can be used to quantitatively describe the synchronisation of oscillators via the order parameter R described by equation 11 (1986). The order parameter approaches 1 as the oscillations increasingly synchronise and is close to 0 when the oscillators have uniformly distributed random phases.

(11) $$R(t) = \frac{1}{N_s} \left| \sum_j^{N_s} e^{i\varphi_j(t)} \right|$$

Research by A. Weber et al. has applied this model to glycolytic oscillations in yeast before to study glycolytic synchronization and desynchronization by looking at NADH fluorescence (2012), (2020).

The instantaneous phase is required to compute the order parameter. Hence, the intracellular NADH concentration over time was exported from the simulations. A representative sample of 250 parcels is taken. The mean is subtracted from the signal to remove the zero-frequency component. A Fourier band pass filter is used to extract the fundamental frequency of the NADH signal and eliminate higher frequency harmonics which can influence the instantaneous phase of the signal. The signal is padded on both sides with zeros for one signal length due to the discrete nature of the transform.

The instantaneous phase $\varphi(t)$ of the glycolytic oscillations is found by taking the argument of analytical signal $x_a(t)$ computed using the SciPy Hilbert transform function from the filtered signal $x(t)$ (equations 12). The full data analysis code can be found in appendix 4.

(12.1) $$x_a(t) = x(t) + i\tilde{x}(t)$$

(12.2) $$\tilde{x}(t) = H[x(t)]$$

(12.3) $$x_a(t) = x_m(t)e^{i\varphi(t)}$$

(12.4) $$\varphi(t) = arg\,[x_a(t)]$$

The cell population will be defined as synchronised when the rank order parameter R exceeds 0.8, below this value the population is either partially ($R > 0.4$) or totally desynchronised ($R \leq 0.4$) (Weber et al., 2020).

Experimental overview and parameters

The research aim of this thesis is to reproduce the results of Lapin et al. 2004 using *LBM* simulation and to show that two-way coupled *EL* simulations with metabolic network simulation are feasible using this method.

First, the physical validity of the *LBM LES* simulation will be established by comparing the power number to literature results at various resolutions. It should be noted that while the resolution-independent power number is useful for establishing the physical validity of the model, simulations do not have to be run at such high resolutions. Lower resolutions can be used so long as flow-behaviour is good.

Furthermore, the variables affecting particle distribution will be investigated. Due to software limitations in M-Star, inertial particles must be used. Particle accumulation due to their inertia must be avoided, since inertial particles are not necessarily flow-following like the particles used in Lapin's model (Henríquez Lira et al., 2021). Though a follow-up paper by Lapin et al. in 2006 showed that some amount of accumulation does occur due to flaws in the *DRW* turbulence model.

Finally, the factors affecting synchronisation and desynchronisation of the simulated glycolytic oscillations will be determined and compared to Lapin's original model.

The tables below are used as reference for the various simulations with the adjusted parameters. Each table-based grouping of cases has an associated base case description. Simulation resolution is defined as the number of spatial subdivisions.

Table 4. Simulation parameter for power number determination.

Case	Resolution [-]
PO50	50
PO100	100
PO150	150
PO200	200
PO250	250
PO300	300
PO350	350

For the power number determination, the simulation was run for 90 seconds with a stirring speed of 55 RPM. The first 45 seconds allowed for the fluid to attain steady state in terms of kinetic energy. No parcels were included in these simulations to reduce computations times. The averages of the dissipation rate and impeller power are taken over the final 45 seconds to establish the average power consumption in steady state.

The Stokes number simulations were run for 90 seconds at a resolution of 100 subdivisions with varying stirring speeds, particle diameters and particle densities. The fit of the particle distribution at 90 seconds is taken. The metabolic model is disabled to reduce computation times of these simulations. Due to the large number of simulations, the tabular data can be found in appendix 2.

Table 5. Simulation parameters for synchronisation and desynchronisation. Blue indicates injection number scaling.

Case	Run time [s]	Resolution [-]	Stirring speed [RPM]	Particle diameter [mm]	Parcel number [-]
D 1 - 4	1500	50 - 200	18.333	5	10^5
D 5 - 8	1500	50 - 200	55	5	10^5
INS 1-4	1500	100	1.833 - 55	0.5	10^5 (× 1000)
PN 1	1500	100	18.333	2.5	1.25×10^4 (× 64)
PN 2	1500	100	18.333	2.5	10^5 (× 8)
PN 3	1500	100	18.333	2.5	8×10^5
LONG18	3600	100	18.333	0.5	10^5
LONG55	3600	100	55	0.5	10^5

The synchronisation and desynchronisation of the parcels were studied under a range of conditions as described by table 5. These simulations generally have a computation time of about an hour to a day depending on resolution and the number of resolved particles. For higher resolutions, storage speeds quickly become the limiting factor.

One requirement to be able to compare the various results is a constant volume fraction of parcels. In all simulations with the metabolic model enabled, the volume fraction is set at 0.1. Reducing the particle diameter would result in a reduction in the volume fraction. Either increasing the number of particles or using the injection number scaling functionality in M-Star can be utilised to counteract this issue. Injection number scaling like the parcel approach described earlier, where one virtual particle represents several real particles represented by the scaling number. All metabolic rates can subsequently be multiplied by this scaling factor when coupling to the extracellular scalar.

When injection number scaling is used, it is necessary to decrease the time step size to maintain the numerical stability of the metabolic network, especially at slower stirring speeds. This contrasts with a previous hypothesis as to the cause of this numerical instability. It was thought that the metabolic and coupling rates would become sufficiently small for the single-precision floating point numbers used in GPUs to start causing floating point errors. However, the expectation would be that smaller time step sizes would worsen the numerical instability, since reducing the time step size results in smaller rates. Thus, further research as to the cause of this instability is required. The associated lowered Courant numbers for the injection number scaled simulation are shown in table 6.

Table 6. Courant numbers used for simulations using injection number scaling.

Case	Stirring speed [RPM]	Courant number [-]
INS 1	1.833	0.0005
INS 2	5.5	0.005
INS 3	18.333	0.01
INS 4	55	0.05

Results & Discussion

Model validation

Numerical testing of *CFD* models is essential to verify whether the applicable physics are valid. The magnitude of the heterogeneities in the bioreactor are dependent on the mixing and thus the impeller action. Verifying the physical validity of the impeller is done via comparing the convergent / grid-independent impeller power number to literature values. The dimensionless power number Po of the impeller is known to be 5.7 for turbulent conditions for $Re_{imp} > 20{,}000$ (Costes & Couderc, 1982, pp. 25–34). Turbulent conditions are defined according to the impeller Reynolds number Re_{imp} (equation 13). The power numbers can be computed either from the torque on the impeller P_{imp} or the total power dissipation P_ϵ using equation 14. The power values themselves are obtained from M-Star, which computes the force balance on the impeller and integrates the local power dissipation rates over the entire control volume. The power values are the average impeller torque power and total power dissipation over 45 seconds after the fluid's kinetic energy is allowed to achieve steady state.

(13) $$Re_{imp} = \frac{N_{imp} d_{imp}^2 \rho_f}{\mu_f}$$

(14) $$Po_{imp} = \frac{P_{imp}}{\rho_f N_{imp}^3 d_{imp}^5} \quad \text{or} \quad Po_\epsilon = \frac{P_\epsilon}{\rho_f N_{imp}^3 d_{imp}^5}$$

As shown in figure 3, the power number based on the energy dissipation Po_ϵ converges to the literature value, being within 5% for resolutions above 200. Notably, for higher resolutions the power number based on the impeller torque power input Po_{imp} increasingly underestimates the power number resulting in a deviation from the dissipation-based power number. This is contrary to what is observed using *FV LES* simulation, which instead show Po_ϵ underestimating experimentally derived power number by a significant amount (Sommerfeld & Decker, 2004), (Yapici et al., 2008). Tabular data is available in appendix 2.

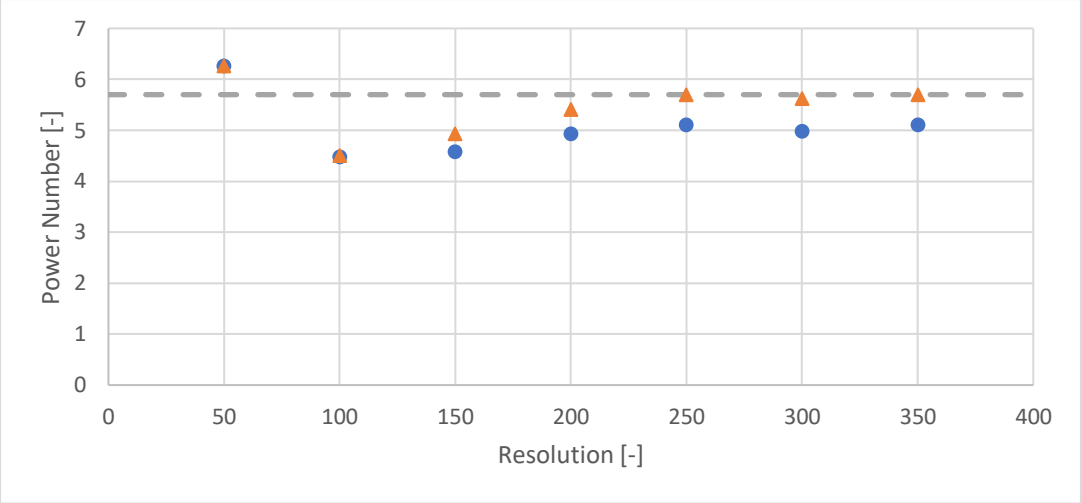

Figure 3. The power number based on the impeller power input (blue cirlces) and the energy dissipation (orange triangles) over the resolution derived from simulations PO1-7. The gray dashed line indicates the reported literature value (5.7) for this reactor by Costes and Couderc. Stirring speed at 55 RPM, resulting in $Re_{imp} \approx 20{,}000$.

Due to time limitations, a resolution of 100 was chosen for most simulations. While less accurate in terms of the simulated turbulence, the overall flow field is deemed sufficiently high resolution to simulate particle movement.

Particle distribution

Microbial cells can be considered massless flow-following particles due to their small size, low mass, and neutral buoyancy. This assumption was also used by Lapin et al. However, due to software limitations within M-Star, particles with mass are required to be able to implement the metabolic network model. Consequently, the resulting inertial particles are not per definition flow following as opposed to tracer particles.

The degree of flow following can be quantified via the Stokes number Stk, which is defined as the ratio between the characteristic relaxation time of the particle as governed by inertia and the characteristic time scale of fluid flow. Particles with a Stokes number above unity show inertial behaviour and hence do not conform to local flow field.

The uniformity of particle distribution in isotropic turbulence is highly dependent on the Stokes number (Eaton & Fessler, 1994). The particle distributions in vortices become highly non-uniform when the Stokes number using the characteristic time of vortex is close to unity. This was shown in research by R.C. Hogan and J.N. Cuzzi by comparing the simulated particle distribution to the expected uniform particle distribution at various Stokes numbers (2001). M-Star has inbuilt particle distribution data calculations which include a goodness of fit model for the distribution of the Nearest-Neighbour distances against the uniform distribution (M-

Star Simulations LLC, 2022). The uniform distribution has a probability density function $PDF(r)$ based the mean distance a as shown in equations 15.

$$\bar{r} = \left(\frac{3V_f}{4\pi N_p}\right)^{\frac{1}{3}} \quad (15.1)$$

$$PDF(r) = \frac{3}{\bar{r}}\left(\frac{r}{\bar{r}}\right)^2\left[1-\left(\frac{r}{\bar{r}}\right)^3\frac{1}{N_p}\right]^{N_p-1} \quad (15.2)$$

Furthermore, inertial centrifugal movement of the particles at high Stokes numbers in curved pipes has been shown to cause accumulation at the tube walls when using the primary centrifugal time scale t_ω (Henríquez Lira et al., 2021). Similar accumulation at the tank walls in the stirred tank reactor at high Stokes numbers can be shown by looking at the volume fraction compared to the expected volume fraction of 0.1 and the distribution of nearest neighbour distances in relation to the expected distribution. Conversely, such accumulation is absent when smaller particle sizes are used resulting in lower Stokes numbers (figure 4).

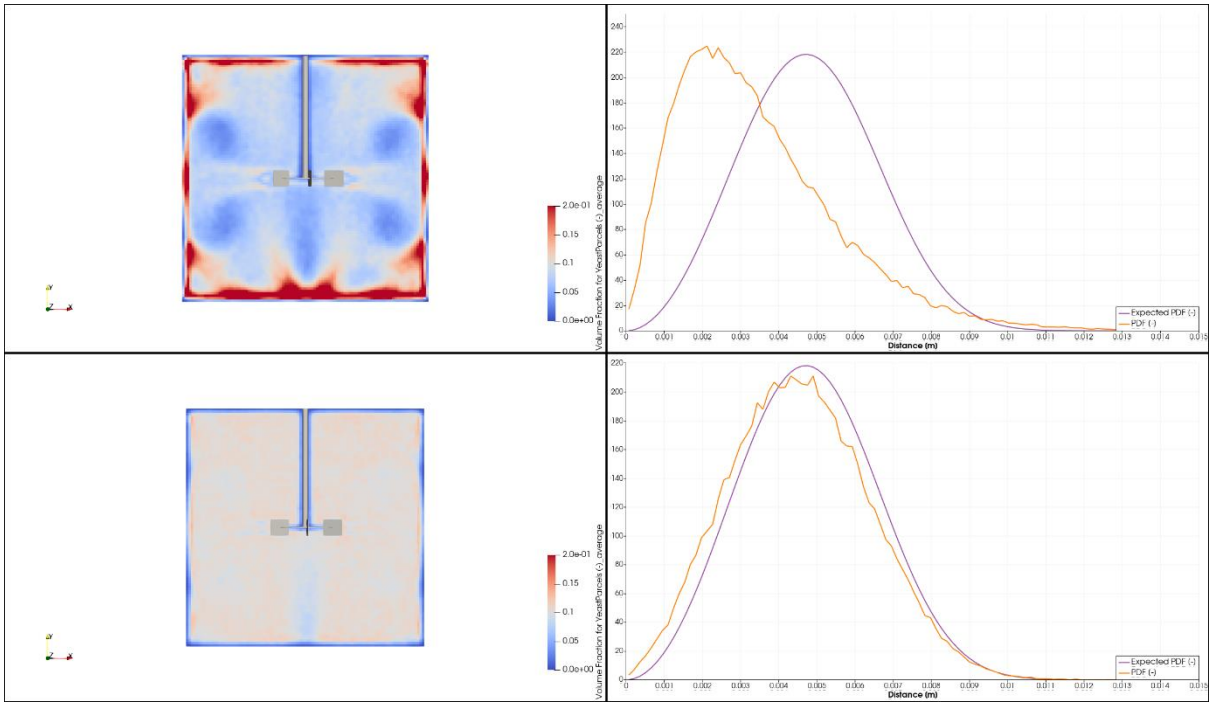

Figure 4. Volume fraction and nearest-neighbor distribution of the particles in a waterlike fluid. Top: particle diameter 5 mm, N_{imp} 18.333 RPM. Bottom: particle diameter 0.5 mm, N_{imp} 18.333 RPM. The resolution of the simulations was 100.

The primary centrifugal Stokes number is calculated using equation 16. The characteristic fluid time is the inverse of the angular velocity of the impeller.

$$Stk_\omega = \frac{t_p}{t_\omega} = \frac{\rho_p d_p^2 \omega_{imp}}{18\mu_f} \quad (16)$$

Assuming both the non-uniformity with a Stokes number close to unity and the wall accumulation are effects present in the simulations. The expectation is for the particle distribution to be highly non-uniform when the Stokes number is at and above unity and increasingly uniform when Stokes numbers is below unity.

First, the M-Star fit value after 90 seconds of simulation is inverted and normalised so that 1 is defined as the fit at $Stk_\omega = 1$ and 0 is the fit of a uniform particle distribution. The normalised fit is plotted against the Stokes number in figure 5. Poor distribution occurs at a Stokes number around and above unity and better distribution at Stokes numbers below unity which is in line with expectation. Tabular data is available in appendix 3.

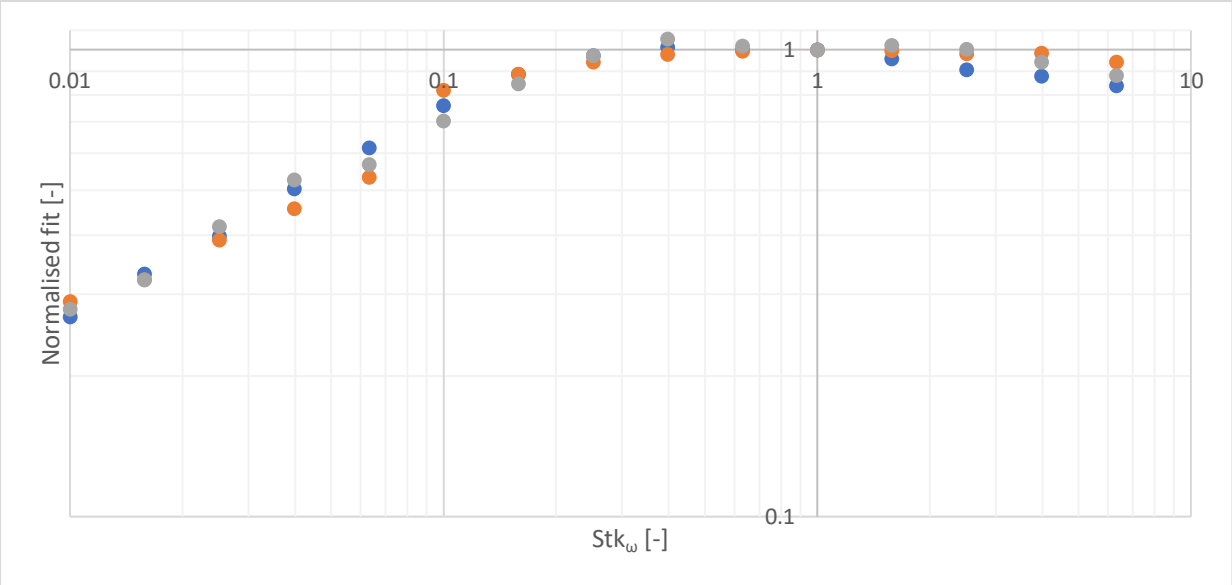

Figure 5. The primary centrifugal Stokes number against the normalized fit with the ideal particle distribution. Fit is normalized by defining the fit as 1 at $Stk_\omega = 1$. The resolution of the simulations was 100.

The particle distribution can thus be made more uniform via reducing the primary centrifugal Stokes number through lowering the particle density, particle diameter or reducing the stirring speed. Care should be taken when reducing particle diameter to maintain a constant volume fraction. This may be accomplished by applying injection number scaling as stated previously.

One issue faced when comparing our results to those of Lapin 2004, is that the particles are not uniformly distributed in the original model as addressed in Lapin's 2006 paper. The *DRW* model used in the original paper results in unrealistically long residence times near the tank walls (Lapin et al., 2006). This implies a higher particle concentration near the tank walls in the 2004 model, though Lapin did not plot the particle distribution. Consequently, the metabolic rates coupled to the scalar are

heterogeneously distributed. This may lead to a more heterogenous scaler distribution, which would in turn affect parcel synchronisation.

Synchronisation and desynchronisation

Simulations were run with various simulation parameters as shown in the methods section to identify the conditions necessary for synchronisation and desynchronisation.

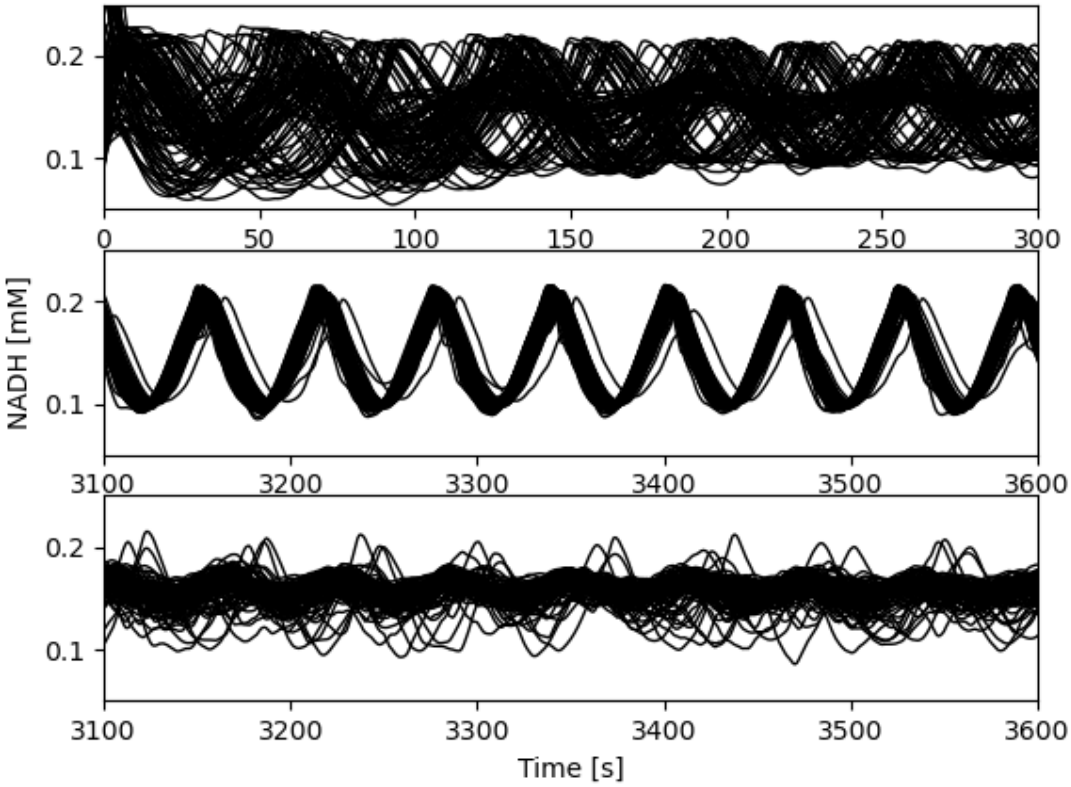

Figure 6. The intracellular NADH concentrations of 250 sampled cells over time. Top subfigure depicting the unsynchronized glycolytic of simulation LONG55 during the first 5 minutes. Middle subfigure containing the synchronised oscillations after 55 minutes of simulation LONG55. Bottom subfigure depicting the desynchronised oscillations after 55 minutes of simulation LONG18.

A stirring speed of 55 RPM appears to be sufficient to cause synchronisation of the glycolytic oscillations (figure 6) contrary to the original model by Lapin where 55 RPM resulted in desynchronisation, and 165 RPM was used to attain synchronisation. This is supported by plotting the rank order parameter R over time (figure 7). Several effects could be responsible for the faster synchronisation in the *LBM* model, including the different turbulence models *LES* and *RANS* affecting scalar transport and the differing particle distributions. Reducing the stirring speed by a third to 18.333 RPM results in a varying degree of desynchronisation apart

from the model using a resolution of 50. Desynchronisation appears to be strongly grid dependent as at higher resolutions the particles desynchronise far more readily.

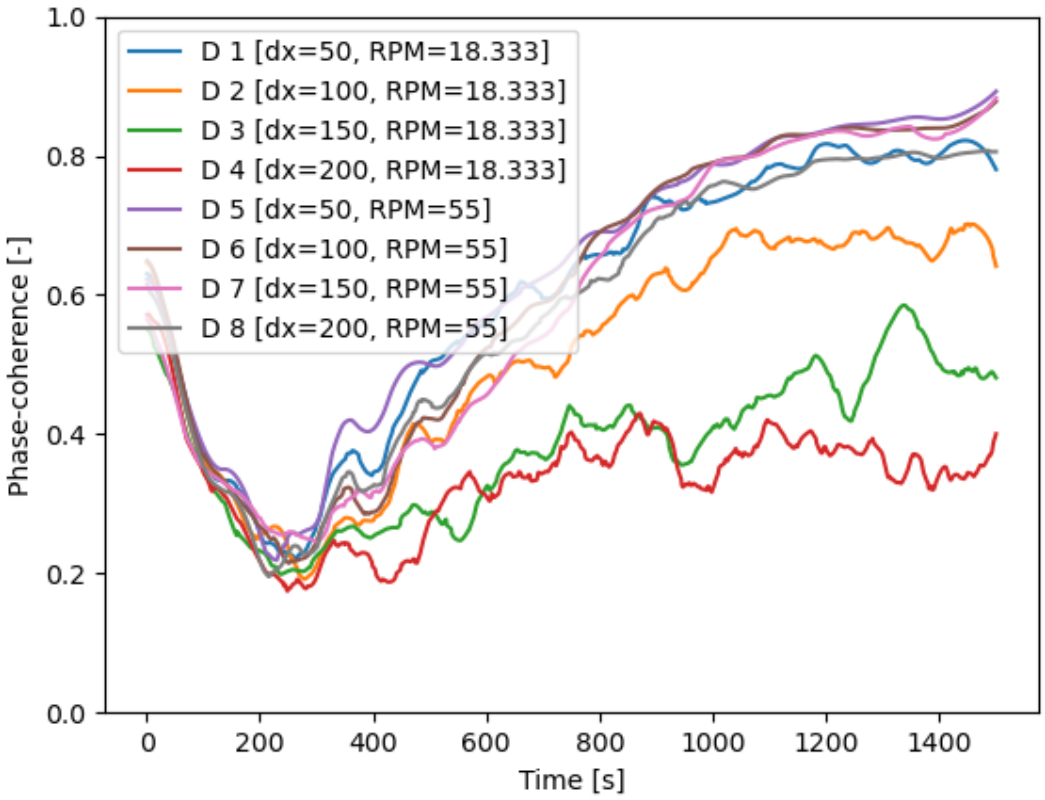

Figure 7. Phase-coherence in the form of the Kuramoto order parameter over time at different resolutions [dx] and stirring speeds [RPM].

Reducing the particle size using injection number scaling results in a more uniform particle distribution as shown previously. This results in requiring far slower stirring speeds to attain desynchronisation as shown in figure 8. This indicates that non-homogeneous particle distribution is essential to allowing desynchronisation in the *LBM* model. This effect can be explained by the spatially heterogenous metabolic rates leading to a heterogeneous scalar concentration. Parcels will desynchronise more readily, due to being exposed to these heterogenous conditions. The implication is that the flawed particle distribution because of the *DRW* turbulence model may have been essential to achieving the results presented in the original Lapin paper. Moreover, the particle distribution being a dominant effect can explain the differences in required stirring speed for desynchronisation detailed previously.

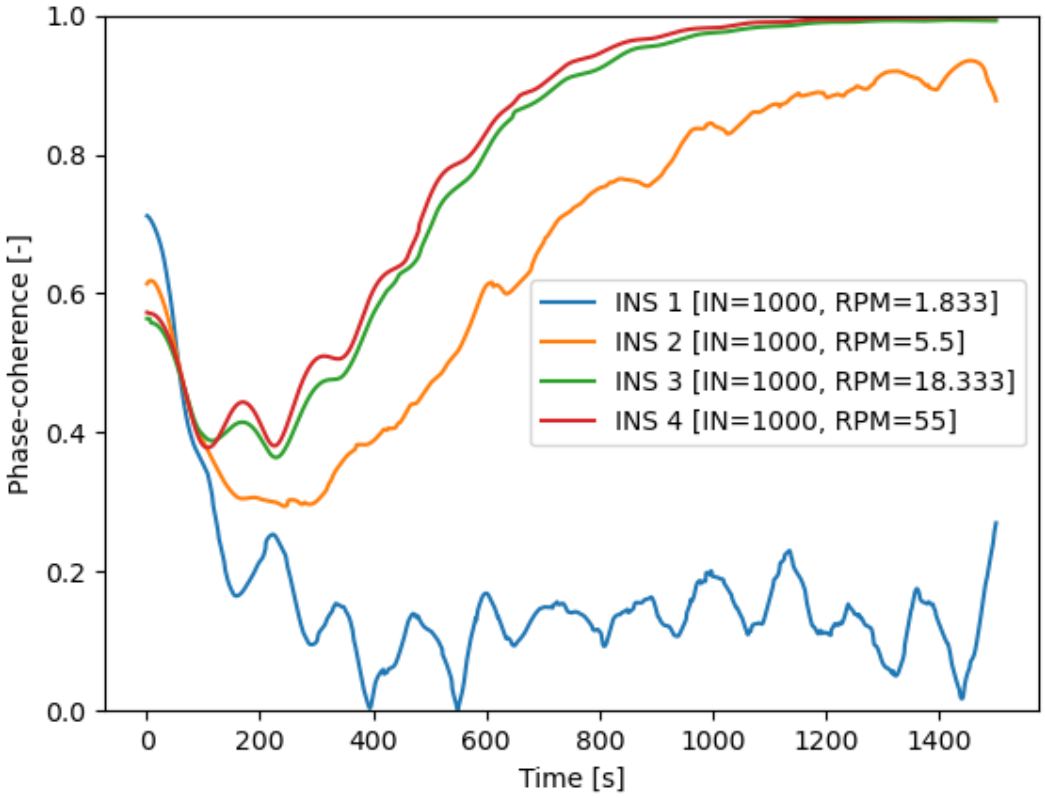

Figure 8. Phase-coherence in the form of the Kuramoto order parameter over time at different stirring speeds using injection number scaling. The resolution of the simulations was 100.

The strong grid dependence of synchronisation is an interesting unexplained effect. The current hypothesis is based on a paper by Haringa et al. describing setup guidelines for *EL* simulations (2017). Specifically, deriving a relationship between the resolution of the Eulerian phase through grid cell volume and the number of parcels in the Lagrangian phase.

If the overall metabolic rates are kept constant while the number of particles is reduced, the instantaneous biomass concentration and consequently the local scalar concentration will start to deviate significantly from the surrounding medium. This Lagrangian heterogeneity is essentially equivalent to running the simulation at too low a "Lagrangian resolution". As a result, from the perspective of the simulated parcel, it may experience artificial scalar concentrations leading to spurious deviations in the metabolic network state. Running simulations at higher Eulerian fluid resolutions results in a smaller volume at any specific lattice point or grid cell. Thus, the instantaneous scalar at the parcel location will deviate more readily.

The hypothesis is that higher fluid resolutions and lower particle numbers will result in larger deviations in the local scalar concentration which would shield the parcels from the overall bulk fluid scalar concentration. As a result, one would expect to observe the parcels desynchronise more readily. To test this hypothesis, particle numbers are varied by a factor of 8, while particle diameter and metabolic rates are kept constant using injection number scaling. The expectation is that reducing the number of parcels will result in faster desynchronisation.

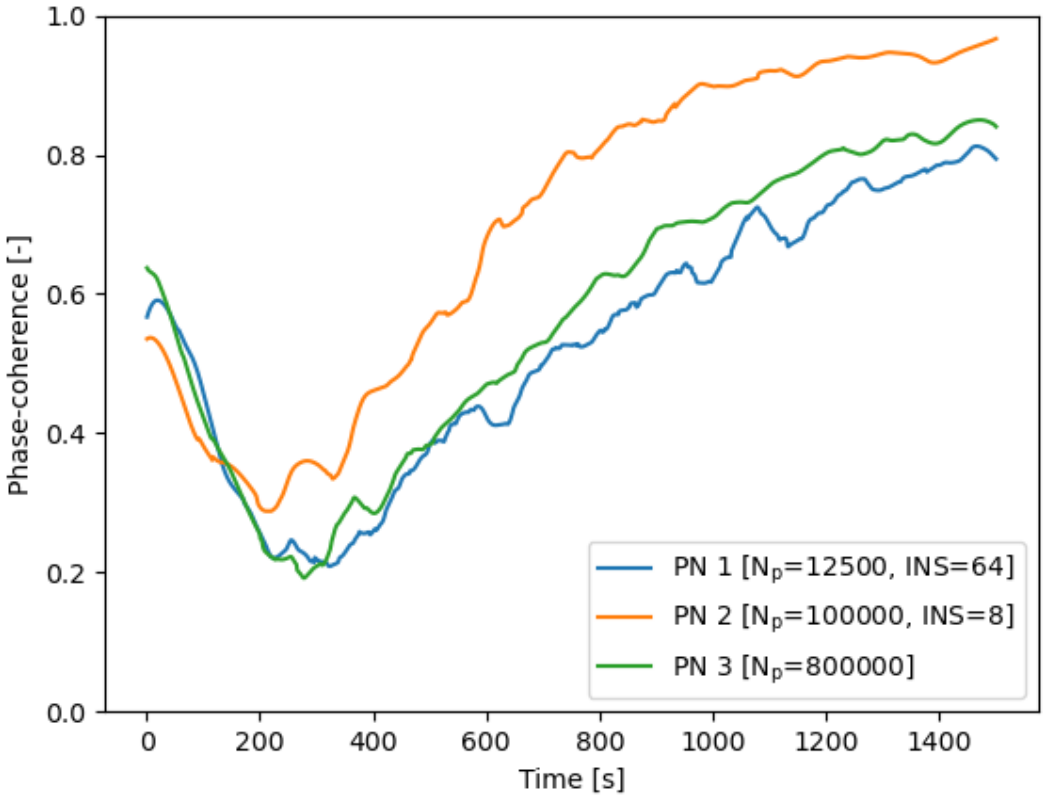

Figure 9. Phase-coherence in the form of the Kuramoto order parameter over time with different numbers of parcels N_p. The resolution of the simulations was 100 subdivisions.

The expected decrease in synchronisation for lower parcel numbers is not observed as illustrated by figure 9. The case with a strongly reduced parcel number PN 1 produces only slightly lower synchronisation than the fully resolved simulation PN 3 and the results for PN 1 are far closer to the fully resolved simulation than the intermediate simulation PN 2. One possible explanation for the absence of expected particle number effect is the non-uniform particle distribution. The shielding effect may be strongly diminished due to the accumulation of parcels at the tank walls since the average distances between parcels are considerably reduced. Additional research into the relationship between the fluid resolution and particle number is required.

Conclusion

To conclude, the goal this Bachelor thesis was to reproduce the results of Lapin et al. 2004 using *LBM* simulation and to show that two-way coupled *EL* simulations with metabolic network simulation are feasible using this method. Furthermore, we discussed and attempted to explain the differences between the original model and *LBM* model in terms of both setup and results. We also explored the pitfalls in model validity influencing the results, such as grid dependence, the effects of heterogeneous particle distributions and the effects of particle numbers.

The comparison between literature data on the reactor vessel and the simulated vessels using power numbers demonstrates that our model can produce sufficiently physically accurate results in terms of fluid mechanics.

A non-homogenous particle distribution appears to be an important factor in causing the heterogeneities responsible for desynchronisation. The unintentional heterogeneity of particle distribution using the *DRW* turbulence model may have played an important role in the results reported by Lapin et al. The particle distribution can be correlated with the primary centrifugal Stokes number showing that lower Stokes numbers result in less heterogeneity due to less accumulation of particles at the vessel walls.

Slower stirring speeds are required to observe the same desynchronisation as seen in Lapin 2004. Once it is observed, it is strongly grid dependent. As stated previously, the synchronisation and desynchronisation rates of the parcels appear to be strongly influenced by the non-uniform particle distribution. This appears to be the factor responsible for the differences between the two models. Though the differences in turbulence models for scalar transport in the form of the Reynold's assumption may also play a role.

Further investigations into resolution effects of the Lagrangian phase by changing the particle numbers did not yield conclusive results. A possible explanation for these results is the non-uniform particle distributions within the *LBM* model. This invites further research into particle number requirements for valid *EL* simulation using *LBM*, like the research performed for *FV RANS* models (Haringa et al., 2017).

Overall, we were able to reproduce the synchronisation and desynchronisation of glycolytic oscillations based on stirring speed as observed in Lapin et al. 2004 using *EL* methods in an *LBM LES* model.

Recommendations

Fundamentally, Lapin's model is difficult to validate. The kinetic parameters of the metabolic network are not based on experimental data. The properties of the flow field are also not verified via comparisons to experimental data. As a result, comparisons of the *LBM* model to experimental data are also limited. Lapin et al. 2006 provides a similar model more grounded in experimental data and would therefore serve as a better model in terms of validation using experimental data. Such a model could be readily implemented by building on top of this study's existing model.

Furthermore, new research could focus on additional simulations and experimental validation of the relation between the Stokes number and particle distribution in stirred tank reactors. Other characteristic fluid times, such as the circulation time, can be explored to see whether they improve the degree of correlation (Henríquez Lira et al., 2021). Likewise, researching the effect of a heterogeneously distributed Lagrangian microbial phase may provide useful insights in research concerning non-uniform biomass distribution such as granular sludge reactors.

As stated previously, the establishment of proper setup guidelines for *LBM LES* simulations to address the issues of grid dependence are essential for physically valid results, like the research performed for *FV RANS* models (Haringa et al., 2017). Glycolytic oscillations in yeast do not necessarily inspire further research as they do not appear to be relevant in bioprocess engineering yet do provide an interesting model for reactor heterogeneity. On the other hand, the use of *LBM* in *EL* simulations and "scale-down" design is very promising as has been demonstrated by this study. The ability to run a two-way coupled *EL* simulation with a dynamic flow field in only about a day, even at relatively high resolutions, is extremely useful in both research and industrial application.

References

Bertram, R., Sherman, A., & Satin, L. S. (2010). Electrical Bursting, Calcium Oscillations, and Synchronization of Pancreatic Islets. *Advances in Experimental Medicine and Biology*, 261–279. https://doi.org/10.1007/978-90-481-3271-3_12

Bier, M., Bakker, B. M., & Westerhoff, H. V. (2000). How Yeast Cells Synchronize their Glycolytic Oscillations: A Perturbation Analytic Treatment. *Biophysical Journal*, *78*(3), 1087–1093. https://doi.org/10.1016/s0006-3495(00)76667-7

Costes, J., & Couderc, J. (1988). Study by laser Doppler anemometry of the turbulent flow induced by a Rushton turbine in a stirred tank: Influence of the size of the units—I. Mean flow and turbulence. *Chemical Engineering Science*, *43*(10), 2751–2764. https://doi.org/10.1016/0009-2509(88)80018-6

Costes, J., & Couderc, J. P. (1982). Pumping capacity and turbulence intensity in baffled stirred tanks; influence of the size of the pilot unit. In H. S. Stephens & D. H. Goodes (Eds.), *Proceedings of the 4th European Conference on Mixing*.

Eaton, J., & Fessler, J. (1994). Preferential concentration of particles by turbulence. *International Journal of Multiphase Flow*, *20*, 169–209. https://doi.org/10.1016/0301-9322(94)90072-8

Eichenauer-Herrmann, J., & Herrmann, E. (1997). Compound cubic congruential pseudorandom numbers. *Computing*, *59*(1), 85–90. https://doi.org/10.1007/bf02684405

Gillissen, J. J. J., & Van den Akker, H. E. A. (2012). Direct numerical simulation of the turbulent flow in a baffled tank driven by a Rushton turbine. *AIChE Journal*, *58*(12), 3878–3890. https://doi.org/10.1002/aic.13762

Gualtieri, C., Angeloudis, A., Bombardelli, F., Jha, S., & Stoesser, T. (2017). On the Values for the Turbulent Schmidt Number in Environmental Flows. *Fluids*, *2*(2), 17. https://doi.org/10.3390/fluids2020017

Haringa, C. (2022). An analysis of organism lifelines in an industrial bioreactor using Lattice-Boltzmann CFD. *Engineering in Life Sciences*. https://doi.org/10.1002/elsc.202100159

Haringa, C., Mudde, R. F., & Noorman, H. J. (2018). From industrial fermentor to CFD-guided downscaling: what have we learned? *Biochemical Engineering Journal*, *140*, 57–71. https://doi.org/10.1016/j.bej.2018.09.001

Haringa, C., Noorman, H. J., & Mudde, R. F. (2017). Lagrangian modeling of hydrodynamic–kinetic interactions in (bio)chemical reactors: Practical implementation and setup guidelines. *Chemical Engineering Science*, *157*, 159–168. https://doi.org/10.1016/j.ces.2016.07.031

Haringa, C., Tang, W., Deshmukh, A. T., Xia, J., Reuss, M., Heijnen, J. J., Mudde, R. F., & Noorman, H. J. (2016). Euler-Lagrange computational fluid dynamics for (bio)reactor scale down: An analysis of organism lifelines. *Engineering in Life Sciences*, *16*(7), 652–663. https://doi.org/10.1002/elsc.201600061

Haringa, C., Vandewijer, R., & Mudde, R. F. (2018a). Inter-compartment interaction in multi-impeller mixing: Part I. Experiments and multiple reference frame CFD. *Chemical Engineering Research and Design*, *136*, 870–885. https://doi.org/10.1016/j.cherd.2018.06.005

Haringa, C., Vandewijer, R., & Mudde, R. F. (2018b). Inter-compartment interaction in multi-impeller mixing. Part II. Experiments, sliding mesh and large Eddy simulations. *Chemical Engineering Research and Design*, *136*, 886–899. https://doi.org/10.1016/j.cherd.2018.06.007

Henríquez Lira, S., Torres, M. J., Guerra Silva, R., & Zahr Viñuela, J. (2021). Numerical Characterization of the Solid Particle Accumulation in a Turbulent Flow through

Curved Pipes by Means of Stokes Numbers. *Applied Sciences*, *11*(16), 7381. https://doi.org/10.3390/app11167381

Henson, M. A., Müller, D., & Reuss, M. (2002). Cell population modelling of yeast glycolytic oscillations. *Biochemical Journal*, *368*(2), 433–446. https://doi.org/10.1042/bj20021051

Hogan, R. C., & Cuzzi, J. N. (2001). Stokes and Reynolds number dependence of preferential particle concentration in simulated three-dimensional turbulence. *Physics of Fluids*, *13*(10), 2938–2945. https://doi.org/10.1063/1.1399292

Krüger, T., Kusumaatmaja, H., Kuzmin, A., Shardt, O., Silva, G., & Viggen, E. M. (2016). *The Lattice Boltzmann Method: Principles and Practice*. Springer Publishing.

Lapin, A., Müller, D., & Reuss, M. (2004). Dynamic Behavior of Microbial Populations in Stirred Bioreactors Simulated with Euler−Lagrange Methods: Traveling along the Lifelines of Single Cells. *Industrial &Amp; Engineering Chemistry Research*, *43*(16), 4647–4656. https://doi.org/10.1021/ie030786k

Lapin, A., Schmid, J., & Reuss, M. (2006). Modeling the dynamics of E. coli populations in the three-dimensional turbulent field of a stirred-tank bioreactor—A structured–segregated approach. *Chemical Engineering Science*, *61*(14), 4783–4797. https://doi.org/10.1016/j.ces.2006.03.003

Madsen, M. F., Danø, S., & Sørensen, P. G. (2005). On the mechanisms of glycolytic oscillations in yeast. *FEBS Journal*, *272*(11), 2648–2660. https://doi.org/10.1111/j.1742-4658.2005.04639.x

Monod, J. (1949). THE GROWTH OF BACTERIAL CULTURES. *Annual Review of Microbiology*, *3*(1), 371–394. https://doi.org/10.1146/annurev.mi.03.100149.002103

M-Star Simulations LLC. (2022). *M-Star CFD documentation*. https://docs.mstarcfd.com/

Nagaosa, R. (1999). Direct numerical simulation of vortex structures and turbulent scalar transfer across a free surface in a fully developed turbulence. *Physics of Fluids*, *11*(6), 1581–1595. https://doi.org/10.1063/1.870020

Osaki, S., Hayashi, K., Kimura, H., Seta, T., Sasayama, T., & Tomiyama, A. (2021). Numerical Simulations of Flows in a Cerebral Aneurysm Using the Lattice Boltzmann Method with the Half-Way and Interpolated Bounce-Back Schemes. *Fluids*, *6*(10), 338. https://doi.org/10.3390/fluids6100338

Pope, S. B. (2000). *Turbulent Flows*. Cambridge University Press.

Schaefer, U., Boos, W., Takors, R., & Weuster-Botz, D. (1999). Automated Sampling Device for Monitoring Intracellular Metabolite Dynamics. *Analytical Biochemistry*, *270*(1), 88–96. https://doi.org/10.1006/abio.1999.4048

Shinomoto, S., & Kuramoto, Y. (1986). Phase Transitions in Active Rotator Systems. *Progress of Theoretical Physics*, *75*(5), 1105–1110. https://doi.org/10.1143/ptp.75.1105

Sommerfeld, M., & Decker, S. (2004). State of the Art and Future Trends in CFD Simulation of Stirred Vessel Hydrodynamics. *Chemical Engineering &Amp; Technology*, *27*(3), 215–224. https://doi.org/10.1002/ceat.200402007

Thomas, J. A., Liu, X., DeVincentis, B., Hua, H., Yao, G., Borys, M. C., Aron, K., & Pendse, G. (2021). A mechanistic approach for predicting mass transfer in bioreactors. *Chemical Engineering Science*, *237*, 116538. https://doi.org/10.1016/j.ces.2021.116538

Weber, A., Prokazov, Y., Zuschratter, W., & Hauser, M. J. B. (2012). Desynchronisation of Glycolytic Oscillations in Yeast Cell Populations. *PLoS ONE*, *7*(9), e43276. https://doi.org/10.1371/journal.pone.0043276

Weber, A., Zuschratter, W., & Hauser, M. J. B. (2020). Partial synchronisation of glycolytic oscillations in yeast cell populations. *Scientific Reports*, *10*(1). https://doi.org/10.1038/s41598-020-76242-8

Wolf, J., & Heinrich, R. (2000). Effect of cellular interaction on glycolytic oscillations in yeast: a theoretical investigation. *Biochemical Journal*, *345*(2), 321–334. https://doi.org/10.1042/bj3450321

Yapici, K., Karasozen, B., Schäfer, M., & Uludag, Y. (2008). Numerical investigation of the effect of the Rushton type turbine design factors on agitated tank flow characteristics. *Chemical Engineering and Processing: Process Intensification*, *47*(8), 1340–1349. https://doi.org/10.1016/j.cep.2007.05.002

Appendices

1. *Metabolic Network code*

```
//Ordered the same way as Lapin 2004

//Initilisation constant for Acetaldehyde_Pyruvate
const float AP_init = 1.094e-4; //[M]

//Kinetic parameters
const float J0 = 2.3 / 1000 / 60; //[mM min^-1] --> [M s^-1]
const float k1 = 100 * 1000 / 60; //[mM^-1 min^-1] --> [M^-1 s^-1]
const float k2 = 6.00 * 1000 / 60; //[mM^-1 min^-1] --> [M^-1 s^-1]
const float k3 = 16.0 * 1000 / 60; //[mM^-1 min^-1] --> [M^-1 s^-1]
const float k4 = 100 * 1000 / 60; //The weird one: now in [M^-1 s^-1]
const float k5 = 1.28 / 60; //[min^-1] --> [s^-1]
const float k6 = 12.0 * 1000 / 60; //[mM^-1 min^-1] --> [M^-1 s^-1]
const float Q = 4.00; //[-]
const float KI = 0.520 / 1000; //[mM] --> [M]
const float NADHtotm =  1.00 / 1000; //[mM] --> [M]
const float ATPtotm = 4.00 / 1000; //[mM] --> [M]

//Instantaneous reaction speeds of the different intracellular reactions
float r1m = k1 * Glucose_p * ATP_p * 1/(1+powf(ATP_p/KI, Q));
float r2m = k2 * G3P_DHP_p * (NADHtotm-NADH_p);
float r3m = k3 * BPG_13_p * (ATPtotm-ATP_p);
float r4m = k4 * Acetaldehyde_Pyruvate_p * NADH_p;
float r5m = k5 * ATP_p;
float r6m = k6 * G3P_DHP_p * NADH_p;

if (t==0){
    //Initilisation at t=0 to set the intracellular concentration
    //pseudorandom number generator using particle location at t=0 as seed
    union Seed {
        unsigned long int i;
        float f;
    } data;

    data.f = x_p;
    data.i = data.i * 15485863;
    data.i = (data.i * data.i * data.i) % 214748368;
    float rand_a = (float) data.i / 214748368;

    data.f = y_p;
    data.i = data.i * 15485863;
    data.i = (data.i * data.i * data.i) % 214748368;
    float rand_b = (float) data.i / 214748368;

    data.f = z_p;
    data.i = data.i * 15485863;
    data.i = (data.i * data.i * data.i) % 214748368;
    float rand_c = (float) data.i / 214748368;

    //multiplying the initial intracellular components with a random number in the range [0,
2).
    rate_Glucose_p = (Glucose_p * (int(rand_a*1000) % 1000 - 499) / 500) / dt;
    rate_G3P_DHP_p = (G3P_DHP_p * (int(rand_a*1000000) % 1000 - 499) / 500) / dt;
    rate_BPG_13_p = (BPG_13_p * (int(rand_b*1000) % 1000 - 499) / 500) / dt;
    rate_Acetaldehyde_Pyruvate_amount_p = vol_p * 1000 * n_p * (AP_init + AP_init *
(int(rand_b*1000000) % 1000 - 499) / 500) / dt; //unit conversion required for intra- and
extracellular components.
    rate_NADH_p = (NADH_p * (int(rand_c*1000) % 1000 - 499) / 500) / dt;
    rate_ATP_p = (ATP_p * (int(rand_c*1000000) % 1000 - 499) / 500) / dt;
} else {
    //Total rates of intracellular compounds
    rate_Glucose_p = J0 - r1m;
    rate_G3P_DHP_p = 2*r1m - r2m - r6m;
    rate_BPG_13_p = r2m - r3m;
    rate_Acetaldehyde_Pyruvate_amount_p = vol_p * 1000 * n_p * (r3m-r4m); //unit conversion
required for intra- and extracellular components.
    rate_NADH_p = r2m - r4m - r6m;
    rate_ATP_p = -2*r1m + 2*r3m - r5m;
}
```

2. *Power number tabular data*

Resolution	Impeller input power [W]	Power dissipation [W]	Po_{imp} [-]	Po_{ϵ} [-]
50	0.331	0.331	6.262	6.266
100	0.237	0.238	4.482	4.499
150	0.242	0.261	4.580	4.927
200	0.260	0.286	4.926	5.407
250	0.270	0.301	5.101	5.691
300	0.263	0.297	4.983	5.621
350	0.270	0.301	5.101	5.693

3. *Stokes number tabular data*

Varying particle size:

Case	Particle size [mm]	Stirring Speed [rpm]	Density [kg m^{-3}]	Stk_ω [-]	Normalised Fit [-]
1	0.768	18.333	1000	0.0100	0.268
2	0.966	18.333	1000	0.0158	0.331
3	1.216	18.333	1000	0.0251	0.399
4	1.531	18.333	1000	0.0398	0.504
5	1.928	18.333	1000	0.0631	0.616
6	2.427	18.333	1000	0.1000	0.760
7	3.056	18.333	1000	0.1585	0.885
8	3.847	18.333	1000	0.2512	0.970
9	4.843	18.333	1000	0.3981	1.011
10	6.097	18.333	1000	0.6310	1.000
11	7.675	18.333	1000	1.0000	1.000
12	9.663	18.333	1000	1.5849	0.955
13	12.165	18.333	1000	2.5119	0.906
14	15.314	18.333	1000	3.9811	0.878
15	19.279	18.333	1000	6.3096	0.838

Varying stirring speed:

Case	Particle size [mm]	Stirring Speed [rpm]	Density [kg m^{-3}]	Stk_ω [-]	Normalised Fit [-]
1	0.75	19.200	1000	0.0100	0.288
2	0.75	30.430	1000	0.0158	0.322
3	0.75	48.228	1000	0.0251	0.391
4	0.75	76.437	1000	0.0398	0.457
5	0.75	121.144	1000	0.0631	0.533
6	2.50	17.280	1000	0.1000	0.820
7	2.50	27.387	1000	0.1585	0.885
8	2.50	43.405	1000	0.2512	0.940
9	2.50	68.793	1000	0.3981	0.977
10	2.50	109.029	1000	0.6310	0.993
11	2.50	172.800	1000	1.0000	1.000
12	5.00	68.467	1000	1.5849	0.996
13	5.00	108.513	1000	2.5119	0.980
14	5.00	171.982	1000	3.9811	0.983
15	10.00	68.143	1000	6.3096	0.940

Varying density:

Case	Particle size [mm]	Stirring Speed [rpm]	Density [kg m^{-3}]	Stk_{ω} [-]	Normalised Fit [-]
1	1	18.333	589	0.0100	0.278
2	1	18.333	934	0.0158	0.322
3	1	18.333	1480	0.0251	0.418
4	1	18.333	2345	0.0398	0.527
5	5	18.333	149	0.0631	0.567
6	5	18.333	236	0.1000	0.703
7	5	18.333	373	0.1585	0.846
8	5	18.333	592	0.2512	0.971
9	5	18.333	938	0.3981	1.053
10	5	18.333	1487	0.6310	1.018
11	5	18.333	2356	1.0000	1.000
12	25	18.333	149	1.5849	1.022
13	25	18.333	237	2.5119	1.001
14	25	18.333	375	3.9811	0.940
15	25	18.333	595	6.3096	0.880

4. *Data analysis code*

```
import numpy as np
from scipy import signal
import matplotlib.pyplot as plt
from scipy.fft import fft, ifft, fftfreq

sample_num = 250

def get_phase(data, s_num):
    phases = None
    time = data[np.where(data[:, 1]==0), 0][0, 1:]

    for i in range(s_num):
        print(i)
        s_data = data[np.where(data[:, 1]==i), 2][0, 1:]
        s_data = signal.detrend(s_data, type="constant")
        f_data = fft(np.pad(s_data, len(s_data)))
        freq_bin = fftfreq(len(s_data)*3, 1)
        f_data = np.where(np.abs(freq_bin)<=1.5/60, f_data, 0)
        f_data = np.where(np.abs(freq_bin)>=0.5/60, f_data, 0)
        s_data_filtered = np.real(ifft(f_data))
        h_data = signal.hilbert(s_data_filtered)[len(s_data):2*len(s_data)]
        if phases is None:
                phases = np.empty((s_num, len(s_data)), dtype="cfloat")
        phases[i, :] = h_data/np.abs(h_data)
    return phases, time

print("processing data...")
data1 = np.load("ParticleData.npy")
phase1, time1 = get_phase(data1, sample_num)
del data1
print("data processed!")

print("plotting...")
plt.plot(time1, np.abs(np.sum(phase1, axis=0)/sample_num), label="<para>")
plt.ylim(0, 1)
plt.xlabel("Time [s]")
plt.ylabel("Phase-coherence [-]")
plt.legend()

plt.show()
```